Materials Science & Engineering A 856 (2022) 144041

Contents lists available at ScienceDirect

Materials Science & Engineering A

journal homepage: www.elsevier.com/locate/msea

Impact tension behavior of heavy-drawn nanocrystalline CoCrNi medium entropy alloy wire

Yu Qiao [a,b,c,1], Fu-Hua Cao [a,c,1], Yan Chen [a,c,**], Hai-Ying Wang [a,c], Lan-Hong Dai [a,b,c,d,*]

[a] State Key Laboratory of Nonlinear Mechanics, Institute of Mechanics, Chinese Academy of Sciences, Beijing, 100190, China
[b] CAS Key Laboratory of Mechanical Behavior and Design of Materials, Department of Modern Mechanics, University of Science and Technology of China, Hefei, 230027, China
[c] School of Engineering Science, University of Chinese Academy of Sciences, Beijing, 101408, China
[d] School of Future Technology, University of Chinese Academy of Sciences, Beijing, 101408, China

ARTICLE INFO

Keywords:
High entropy alloy
Wire
Split hopkinson tension bar
High strain rate
Low temperature
Plastic deformation

ABSTRACT

High-strength metallic wire is a vital bearing structure used in many industrial fields. Impact loads often challenge the service safety of metal wire in engineering applications. However, few studies have been made on the dynamic mechanical behavior of metallic wires, especially for newly developed high-entropy alloy wires. By equipping split Hopkinson tension bar (SHTB) with specially designed test fixtures, we have carried out a systematic study on the dynamic deformation behavior of the heavily-drawn CoCrNi medium-entropy alloy (MEA) wire in impact tension at both room and cryogenic temperatures. We show that these millimeter-diameter MEA wires with nano-scale grains can achieve an excellent combination of impact tensile strength and ductility at 293 K and 77 K. More interestingly, we find that the strength and ductility of the MEA wire were enhanced simultaneously with decreasing temperature and increasing strain rate. Detailed microstructure characterizations and molecular dynamics simulations reveal that the increased strength and ductility at coupled high strain and low temperature resulted from the multiplication and thinning of nanoscale twins, which further caused additional strengthening and toughening mechanisms such as stack faulting net and secondary twin. This study highlights the advantage of CrCoNi MEA wire for cryogenic temperature and impact applications and provides an experimental reference for the design and evaluation of high-strength metal wires under such extreme conditions.

1. Introduction

High-strength metallic wires are used as heavy-duty structural components in many engineering industries, such as long-span bridges, special lifting equipment, and impact protection nets [1–7]. Wires are usually wound and braided into wire ropes and mesh, for which high strength is requested (>1 GPa) to allow for a reduction in the diameter of solid wire while maintaining its load-bearing ability. The typical model is cold drawn pearlitic steel wire, which exhibits extremely high strength benefiting from the strong confinement of the cementite layer to dislocations [8,9]. However, this strengthening effect, along with other strengthening mechanisms usually accompanied by a reduction of ductility (called the strength-plastic trade-off dilemma), which not only limits the shaping of industrial components but also reduces service safety. Hence, new metallic wires that possess high strength and sufficient ductility should be developed.

In recent years, high/medium entropy alloys (HEAs/MEAs) have received extensive attention due to their novel design concepts and unique properties [10–20]. Numerous studies have shown that HEAs exhibit extraordinary mechanical properties, such as the great potential to overcome traditional strength-ductility trade-off [21–23], high hydrogen embrittlement resistance [24–26], and self-sharpening [27]. Particularly, CoCrNi-based HEAs/MEAs exhibit a perfect combination of strength and plasticity [28–35], showing a great potential to prepare high-strength and high-plastic alloy wires. For example, Zhang et al. found that $Al_{0.3}$CoCrFeNi HEA wires can exhibit both high tensile strength and ductility at ambient and cryogenic temperatures [36]. Huo et al. fabricated cold-drawn CoCrFeNi HEA wire with a 7.0 mm

* Corresponding author. State Key Laboratory of Nonlinear Mechanics, Institute of Mechanics, Chinese Academy of Sciences, Beijing, 100190, China.
** Corresponding author. State Key Laboratory of Nonlinear Mechanics, Institute of Mechanics, Chinese Academy of Sciences, Beijing, 100190, China.
E-mail addresses: Chenyan@lnm.imech.ac.cn (Y. Chen), lhdai@lnm.imech.ac.cn (L.-H. Dai).
[1] The two authors contributed equally to this paper.

https://doi.org/10.1016/j.msea.2022.144041
Received 12 June 2022; Received in revised form 10 September 2022; Accepted 17 September 2022
Available online 21 September 2022
0921-5093/© 2022 Elsevier B.V. All rights reserved.

diameter, which resulted in high tensile yield strength of 1.1 GPa with a considerably high ductility of 13.6% at room temperature [37]. The maximum tensile strength of 2 GPa with limited ductility was reported in cold-drawn CoCuFeMnNi wire [38]. Besides the high strength, CoCrNiFeMn HEA wires also showed a remarkably high tensile strength and excellent resistance to the hydrogen embrittlement [39]. In view of the outstanding damage tolerance and superior general mechanical than CrMnFeCoNi HEAs, CoCrNi MEA has expected a more promising system for high-performance alloy wire. Our previous studies have revealed the excellent mechanical properties of CoCrNi MEA wires and anomalous size effects at the micron scale [40,41], highlighting the advantage of CoCrNi MEA acting as the parent material of high-performance alloy wire.

Although the deformation behaviors of CoCrNi MEA are extensively researched in both ambient and cryogenic temperatures under quasi-static conditions, the underlying deformation mechanisms have not yet been fully understood under impact loadings, especially for heavy cold-drawn wires that usually exhibit an ultra-fine even nanoscale grain structure like severe plastic deformation materials [42,43]. This is important in engineering applications where wire and its products are often subjected to dynamic loads. For example, in ultra-deep coal mines, the multilayer winding hoist often has friction and impact between wire ropes during the winding process [44]. Furthermore, the local wires of the structure usually undergo deformation at a higher strain rate when the wire-rope fence under the vehicle or rockfall impacts [45,46]. The service safety of alloys under high load rate has always been a critical issue in engineering applications. To accurately evaluate the service safety of HEAs/MEAs wires in impact engineering applications, it is necessary to explore their mechanical behaviors at high strain rates.

Stable and damage-free clamping is a critical technical challenge for wire mechanics testing techniques, especially testing the dynamic mechanical properties of wires on Hopkinson tie rods. In wire-related mechanical experiments, wire fixation devices often have large sizes and complex structures [3,46–49], such as the fixation device used by B. Hopkinson in his early research on the impact tensile of iron wires [47]. Traditional fixtures are difficult to apply directly to Hopkinson bars. This may be one of the reasons for the lack of studies on the dynamic tension of the MEA/HEA and even metal wires, although increasing researches are devoted to the high-speed deformation behaviors of bulk materials of MEA/HEAs [17,50,51].

In this study, CoCrNi MEA wires were successfully fabricated to a diameter of 1 mm using mechanical drawing techniques. By developing a wire clamp and experimental method for split Hopkinson tension bars, we carried out dynamic tensile tests at room temperature and low temperature (77 K). Mechanical responses and microstructure evolutions under different loading conditions are characterized to identify the effects of strain rate and temperature on the deformation mechanism of CoCrNi MEA wires, as detailed in the Results section. In the discussion section, the deformation behaviors of these CoCrNi MEA wires are compared with bulk CoCrNi materials. In addition, the strain rate and temperature effect are analyzed on atomic scale by MD simulations.

2. Material and methods

2.1. Alloy preparation

The equiatomic CrCoNi MEA ingot was produced by smelting high-purity metal mixtures (purity of each component >99.9 wt%) in the vacuum magnetic levitation melting furnace. After being homogenized at 1473 K for 24 h, the ingot was hot forged and swaged at 1423 K more than eight times to a round bar with a diameter of 15 mm. These round bars were further hot-rolled at 1123 K to a diameter of 8 mm, hot-drawn at 1073 K to 2 mm, and subsequently cold-drawn to 1 mm at a speed of 0.5 mm/min. Part of them was further heat-treated at 873 K for 1 h after low temperature recovery at 673 K for 2 h.

2.2. Dynamic wires tensile test method

Two different clamps, called sleeve-type wedge clamps and square wedge clamps, are designed to test cold-drawn wire and heat-treated wire, respectively. The sleeve-type wedge clamp shown in Fig. s1a has a strong clamping ability, but it could not stably clamp the high-plastic clamp wires due to its inability to change dimensional. The square-bolt-type wedge clamp (Fig. s1(c)) containing two wedge clamp blocks allows self-clinching during dynamic deformation, which is employed to hold the heat-treated wires with high strength.

Dynamic tensile tests ($\sim 10^3\ s^{-1}$) were performed on a 12 mm Hopkinson tie bar equipped with high-speed photography (Fig. 1a). The wire sample is protected with an aluminum sheet, forming a "sandwich" structure to prevent damage by the clamps (Fig. 1c and (d)). It should be noted that the difference in cross-sectional area between clamps and Hopkinson bar inevitably affects the measurement of the stress wave, especially the reflected and transmitted wave signals. Since the stress-strain curves are calculated only by incident wave and transmitted wave (two-wave method [52]), the affected reflected waves do not affect the calculated strain. To verify the accuracy of the bar end displacement in the experiment, we used high-speed photography to shoot the experimental process and then calculated the displacement of the incident bar end according to the photos before and after impact. On the other hand, the displacement of the incident bar end is calculated by subtracting the transmitted wave from the incident wave collected in this experiment. The displacement error between the two methods is less than 5%, indicating that the effect of the variable cross-section parts is negligible. Based on elaborated stress wave analysis, see supplementary materials, we have corrected the transmitted wave by superimposing the falling edge of the transmitted wave on the rising edge of the transmitted wave.

The low-temperature dynamic tests are performed in a small-volume liquid nitrogen test box (Fig. 1b). The clamps and samples were assembled before the experiment and immersed in liquid nitrogen to pre-cool for 5 min. The pre-cooled clamps and sample were attached to the Hopkinson bar, and a T-type thermocouple was attached to the sample. To correct the effect of low temperature on the bar, we adopt the previously proposed Hopkinson bar temperature experimental data processing method [53]. Due to the introduction of a closed liquid nitrogen test box, the deformation process of the sample cannot be captured in real time by a high-speed camera. We used a file to create scratches on the black oxide surface of the wire samples as feature point markers. After impact loading, the accurate strain signal of the material is calculated according to the correction method of the room temperature experiment at the position of the calculated mark points.

2.3. Quasi-static test methods and characterization methods

The quasi-static tensile tests (strain rate $\dot{\varepsilon} = 1 \times 10^{-3}\ s^{-1}$) were performed on a material testing machine (UTM4204), where an extensometer measured the strain data. To avoid the wire sample being damaged by the chuck of the testing machine, The clamping parts of the wire samples were protected by two 6061 aluminum alloy sheets. The quasi-static tensile tests were performed at room temperature (293 K) and liquid-nitrogen temperature (77 K).

The dislocation density of the MEA wires was measured by X-ray diffraction (XRD, Rigaku DMAX-RB) and Cu Kα radiation. This work used transmission electron microscopy (TEM; JEM-2100 F) to characterize and analyze the wire sample microstructure after the quasi-static and dynamic tensile tests. The specimens used for TEM observation were obtained by focused ion beam (FIB) processing, and the observation conditions and parameters of the microstructural characterization are described in detail in Section 3.

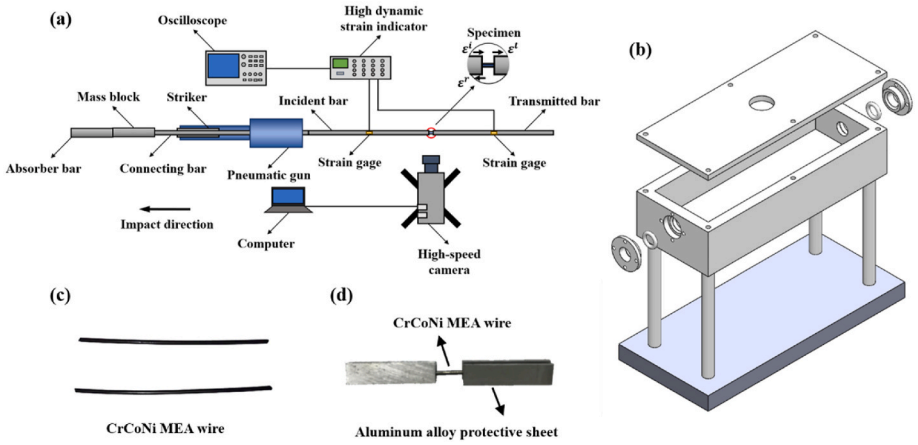

Fig. 1. (a) Schematic diagram of a split Hopkinson tensile bar device with a high-speed camera, (b) low-temperature environmental chamber model, (c) CrCoNi MEA wires, (d) assembly of wire sample and aluminum sheet.

2.4. Simulation method

Three dimensional nanocrystalline CoCrNi samples with mean grain sizes of 15 nm have been constructed using Voronoi method. The samples are containing 439,0000 atoms and 20 grains with randomly orientations. To create the traditional random solid solution structures, Ni atoms in fcc phase were randomly selected and replaced with Co and Cr until the desired composition was achieved. MD simulations were performed using the Large-scale Atomic/Molecular Massively Parallel Simulator (LAMMPS) package [54], where the recently developed DFT-calibrated embedded-atom CrCoNi potential [55] is used. Periodic boundary conditions were applied in all directions to mimic the deformation responses deep in a larger sample. Before uniaxial tension simulation, the samples are thoroughly relaxed with energy minimization and then being equilibrated in an isobaric-isothermal (NPT) ensemble [56] at zero pressure and temperatures of 300 K and 77 k for 10 ps. Uniaxial tensile loadings were simulated at strain rates of $5*10^{7}$–10^{10} s^{-1} at 300 K and 77 k, where the other direction boundaries were allowed to vary to keep the corresponding components of the stress to zero. A program OVITO was employed to visualize the atomic configurations [57], where the local crystalline structure is analyzed by the polyhedral template matching method [58].

3. Results

3.1. Microstructure

The longitudinal grain structure is shown in Fig. 2a and (c) for cold-drawn and heat-treated CrCoNi MEA wire. Although repeated cold drawing resulted in a heavily cold-worked microstructure for which the grain size is difficult to resolve without ambiguity in TEM, the typical polycrystalline diffraction ring detected by the selected area electron diffraction (SAED) pattern (inset of Fig. 2a). It indicates that the grain size of MEA wire is less than 100 nm by multipass cold drawn, which are

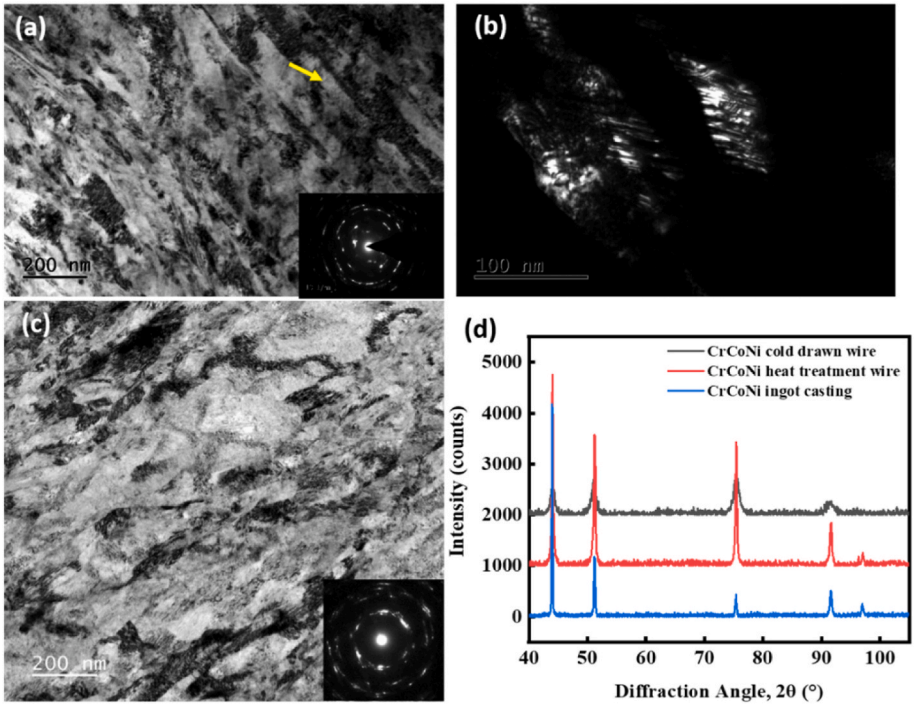

Fig. 2. The TEM micrographs of cold-drawn CoCrNi wire (a) bright field and (b) dark field image; (c) bright field TEM micrographs of heat-treated CoCrNi wire (d) X-ray diffraction spectra for CrCoNi ingot and wires.

distributed in random crystallographic orientations. The enlarged dark-field TEM image of cold-drawn wire also showed that the nano-scaled grain interior is divided by dislocation and twins, suggesting a seriously distorted grain structure, as shown in Fig. 2b. This also meets the apparent heavy deformed microstructure shown in Fig. 2a and c, where entangled dislocation cells and twins were found to be prevalent.

As shown in Fig. 2c, the entangled dislocation cells in the wire are decreased significantly after two-step heat treatment while maintaining the nanocrystalline structure as manifested by the polycrystalline diffraction ring. Fig. 2d shows the XRD spectrums of cold-drawn MEA wire, heat-treated MEA wire, and MEA ingot, where only FCC peaks are shown, indicating that these MEA wires had an entirely FCC crystal structure. However, there are significant differences in the XRD peak width among different samples, reflecting the differences in dislocation density. Specifically, the dislocation densities of cold-drawn MEA wire and heat-treated MEA wire are estimated as $1.35 \times 10^{16}\ m^{-2}$ and $6.93 \times 10^{14}\ m^{-2}$, respectively. These suggest that the heat treatment process used in this work reduces the dislocation density of the MEA wire successfully without changing its nanoscale grain structure.

3.2. Experimental tensile and deformation behaviors at room temperature

Fig. 3 shows the quasi-static and dynamic engineering stress-strain curves of cold-drawn MEA wire and heat-treated MEA wire at 293 K. As shown, the cold-drawn MEA wires exhibit an extremely high ultimate strength of 1938 MPa with limited ductility under quasi-static loading. This ultra-high strength may originate from the nanoscale grain structure with high-density dislocation accumulation caused by repeated cold drawing processes with severe plastic deformation [59–61]. It was exciting to note that the strength further increased to 2111 MPa under dynamic tension with a strain rate of $10^3\ s^{-1}$, which is 8.9% higher than the quasi-static condition, suggesting a noticeable strain rate strengthening effect.

Fig. 4 shows the bright-field TEM images of cold-drawn MEA wires after quasi-static and dynamic tensile at room temperature (293 K). Besides the heavily entangled high-density dislocations inherited from the as-drawn state, some deformation twin is observed in the MEA wire after quasi-static tensile. A close inspection reveals two kinds of twin morphology, including mature twins with a width of ~40 nm (marked by red arrows) and very thin twin embryos (marked by yellow arrows). The high-resolution TEM image of one of these thin twins indicates a width of ~4 nm with about 20 atomic layers (Fig. 4b). Considering the minimal plastic deformation of cold-drawn MEA wires, which are unable to provide sufficient plasticity for twin growing, these mature twins may be formed during the cold-drawn process instead of quasi-static tensile deformation. Nevertheless, the tensile strength of cold-drawn wire is much higher than critical twin stress, allowing the nucleation of new twins. These newly nucleated twins are limited by the negligible plastic strain, manifesting as very thin twin embryos.

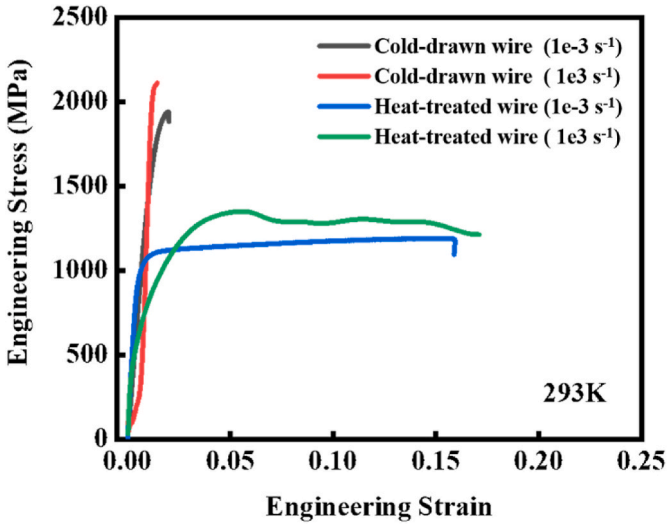

Fig. 3. Quasi-static and dynamic mechanical properties of CoCrNi wires at 293 K.

Similar to quasi-static tensile, a high density of clustered dislocation structures and some deformation twins are also found in the dynamic tensile samples, as shown in Fig. 4c. Comparing the microstructure after dynamic tensile and quasi-static tensile (Fig. 4a and c), we find that the tension induced thin twins after dynamic tension is denser than quasi-static condition. The magnified image of the twinning region shown in Fig. 4d presents some stacking faults, suggesting a dislocation-twin interaction during dynamic loading. High strain rate loading often leads to an inhomogeneous strain within the sample due to the short response time, wherein some regions would exhibit localized plastic events such as dislocation-twin interactions, which widen the twins and increase the strength of cold drawn wire simultaneously.

The high-density entangled dislocations inhibit dislocation motion and thus bring these cold-drawn MEA wires to an ultra-high strength at both quasi-static and dynamic tensile. However, the high-density entangled dislocations in the cold-drawn wires often serve as preference sites for microcrack nucleation [62,63], which leads to fracture at low strain as manifested by the poor ductility at both quasi-static and dynamic tensile. In turn, it suggests that the plasticity of cold-drawn wires can be improved by reducing dislocations.

This inference can be proved by the strain stress behaviors of heat-treated wires tensiled at dynamic and static conditions (seen Fig. 3). Significantly, the ultimate strain of the heat-treated MEA wire reaches~15%, much higher than cold-drawn wire. This suggests that the high plasticity of cold-drawn wire can be obtained by lowing dislocation accumulation, which increases the mobility and free path of dislocations. Although the reduction of dislocation density by heat treatment results in a significant loss of strength, the strength of heat-treated CoCrNi wire remains a relatively high level with a yield strength of 1014 MPa and ultimate strength of 1189 MPa at 293 K. Comparing the quasi-static tensile microstructure of heat-treated (see Fig. 5a) and cold-drawn wire (see Fig. 4a) reveals that the twin lamella in the heat-treated wire is significantly wider than that of cold-drawn wire. These wider twins may originate from the widening of inherited mature twins during heat treatment. Besides, abundant newly tiny twins are present in the heat-treated wire. These suggest that heat-treated microstructure with less entangled dislocation cells allows sufficient nucleation and development of twinning during plastic deformation, which can improve ductility and strength simultaneously.

Similar to the cold-drawn wire, the heat-treated CoCrNi MEA wire also exhibits a noticeable strain rate effect under dynamic tension. As shown, under dynamic stretching at room temperature, the yield strength of heat-treated MEA wire was increased to 1350 MPa, ~30% higher than the quasi-static condition. Besides, the elongation of heat-treated wire is about 16%, slightly higher than that under quasi-static conditions. In short, the heat-treated MEA wire exhibit a significant strain rate strengthing effect without loss of plasticity under dynamic loading.

Fig. 5b presents photomicrographs of heat-treated CoCrNi wires after dynamic tensile loading at room temperature. As shown, the twin lamellas are denser but thinner than quasi-static loading condition, suggesting a higher twin formation capacity under high strain rate. This may originate from the high-stress state during dynamic tension that facilitates the nucleation of twins. Moreover, the thinner feature of twins in the dynamic tested wire is related to their shorter impact time. In addition, dense dislocations are wrapped around these twins, similar to the phenomenon observed in nanocrystalline Ni–Fe dilute alloy [64]. This substantiates that nano twins can hinder dislocations effectively, as well-known twin boundary strengthening. Meanwhile, these highly active deformation nanotwins can accommodate a large amount of

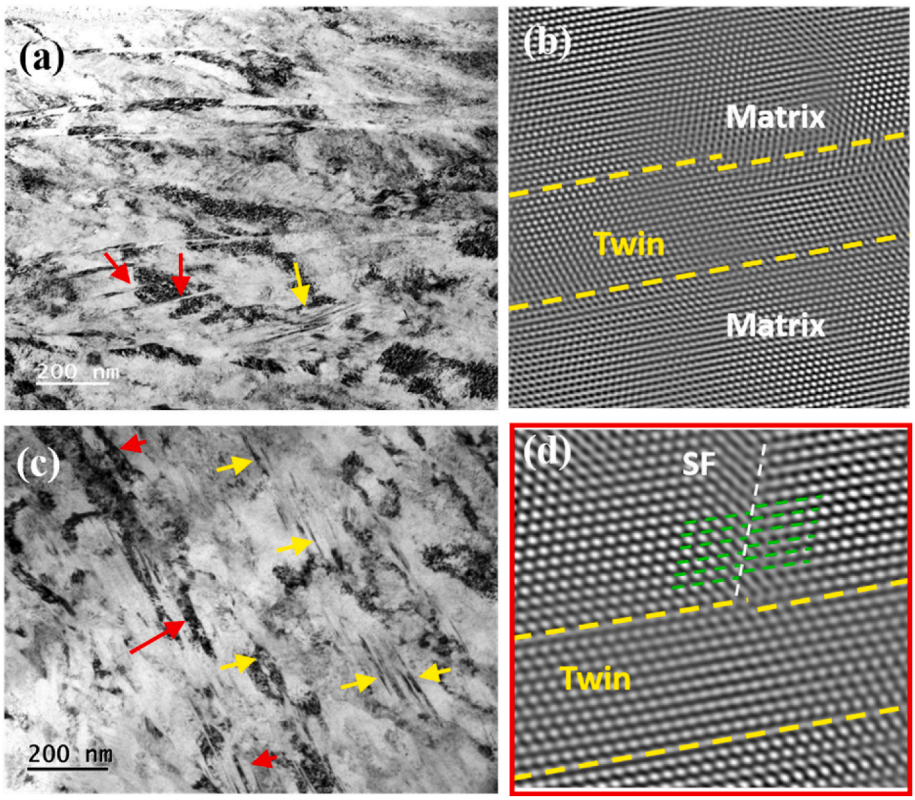

Fig. 4. TEM images of cold-drawn CoCrNi wires after tensile at 293 K. (a) bright-field image after quasi-static deform (b) High-resolution TEM image of twins (c) bright-field of dynamic deformed CoCrNi wire (d) High-resolution TEM image shows atomic detail of the twinning region.

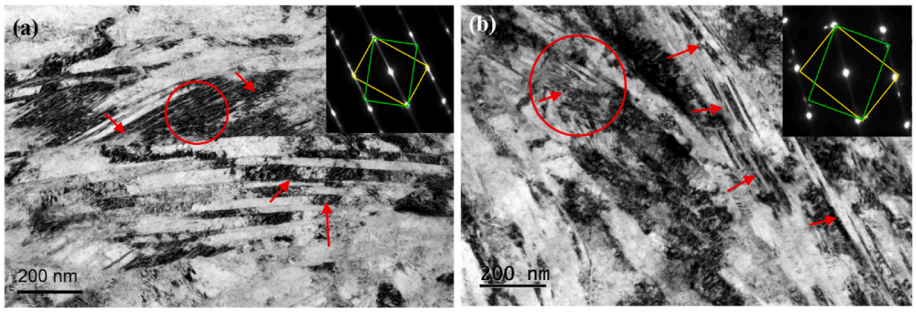

Fig. 5. The bright-field TEM images of heat-treated CoCrNi wires after (a) quasi-static and (b) dynamic tensile at room temperature.

plastic deformation through twin-dislocation interactions, which ensure high plasticity during twin boundary strengthening.

3.3. Experimental tensile and deformation behaviors at cryogenic temperature

Besides strain rate, temperature is another important factor affecting mechanical properties. Fig. 6 demonstrates the quasi-static and dynamic mechanical properties of both cold-drawn and heat-treated CoCrNi wires at 77 K. Compared with room temperature, the strength has increased significantly at 77 k for both dynamic and quasi-static loading. For example, the ultimate strength of cold-drawn MEA wire at 77 K was increased by 27.7%–2475 MPa, and the yield strength was increased by 19.9%–2126 MPa, relative to 273 K.

The thermally activated dislocation behavior is known to be suppressed at low-temperature environments and requires larger stress to promote dislocation movement [65], which results in the higher strengths of the wires studied here. Fig. 7 presents photomicrographs of cold-drawn wires under quasi-static tensile at 77 K. As shown, the nanoscale twin lamellas at low temperatures are thinner and more closely arranged than at room temperature. This suggests that twin appear to be more favorable at cryogenics temperature, which is associte with the lower stacking fault energy at low temperature [66]. Note that this low-temperature strengthening effect is amplified for the heat-treated wires, in which the yield and ultimate strength at 77 K are increased to 1259 MPa and 1617 MPa, respectively, 24.2% and 36.0% higher than the cold-drawn state. Astonishingly, the ultimate strain of heat-treated MEA wire is ~0.3 at 77 K, nearly twice over the elongation of room temperature condition. This excellent strength and plasticity are related to the thinner and denser nano deformation twin bundles (the collection of dense nano-scale twin lamellas) in the heat-treated wire.

The mechanical properties shown in Figs. 3 and 6 confirmed that both high strain rate and low temperature can increase the strength of CoCrNi wires. As expected, the yield and tensile strength are further improved at both high strain rate and cryogenic temperature conditions. The cold-drawn CoCrNi wire exhibits an ultra-high strength of 2662 MPa, which is 7.6% higher than quasi-static loading at cryogenic temperature. For heat-treated wires, the high strain rate also results in a

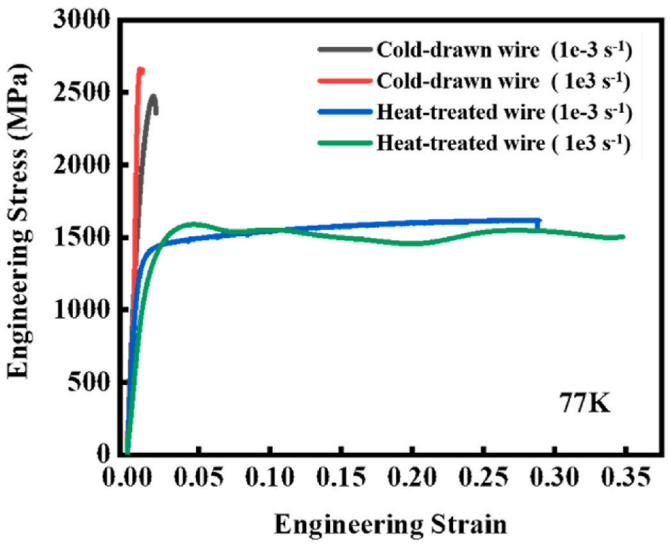

Fig. 6. Quasi-static and dynamic mechanical properties of CoCrNi MEA wires at 77 K.

significant increase of strength at low temperature, accompanied by a substantial improvement of plasticity by 30% than quasi-static loading. Fig. 8a and (b) present the micrographs of cold drawn and heat treated MEA wires after dynamic tensile at 77 K. Selected area diffraction spots show abundant twinning in both cold-drawn and heat-treated MEA wires. A careful comparison between Figs. 8 and 7 reveals that a high strain rate leads to more thinner twins, which hinders dislocation more effectively and hence results in higher strength. Meanwhile, the formation of such high-density twins is accompanied by substantial plastic deformation, leading to a high ductility. Besides, pronounced awn lines are shown on the SAD spots of heat-treated wire, indicating plenty of stacking faults in the twinned region [67,68]. As shown in Fig. 8c, a high density of stacking faults networks are present within these thin twinning bands, in which plenty of L-C locks are formed that can hinder dislocation motion effectively and thus amplify the strengthing effect. These stacking fault networks can also promote twin formation, as mentioned below.

Besides, several secondary deformation twins are found in the heat-treated MEA wires after dynamic tensile at 77 K, as shown in Fig. 8d. The lack of obvious secondary deformation twins at room temperature for both quasi-static and dynamic conditions may relate to room temperature dynamic recovery. The observed secondary twins would introduce more twin interfaces and further refine the grain size, leading to a strong dynamic Hall-Petch strengthening effect since the formation of secondary nanotwins can hinder the dislocation effectively. These secondary nanotwins are related to the high-density dislocations accumulated and tangled at twin boundaries by consuming partial dislocations from these highly distorted regions to release the local stress concentration [64]. In this regard, the formation of secondary nano twins also contributes to the outstanding plasticity in the heat-treated wire after dynamic tensile at 77 K [29,69].

3.4. Atomistic insights into rate and temperature effect

The above experimental results clearly indicate that increase strain rate and decrease temperature can enhance strength significantly without ductility loss. Although strain rate and temperature-related strengthing effects can be comprehended by the thermally activated plastic deformation process, the detailed deformation mechanisms of these nanocrystalline MEA wires are still poorly understood. MD simulations have been widely used to investigate the mechanical properties and plastic deformation mechanisms of nanocrystalline metals, although the inherently high strain rates of MD simulations make it challenging to determine the whole deformation mechanisms occurring in experiments timescale [70–72]. In this section, the dependence of deformation behaviors on strain rate and temperature is discussed based on MD simulation results, which are also compared with experimental results.

Stress-strain curves for nanocrystalline CoCrNi at room temperature and cryogenic temperature are shown in Fig. 9a and Fig. 9b, respectively. It shows a similar stress-strain response as well as strain rate effect between room temperature and cryogenic temperature tension. At strain rate of $5 \times 10^7\ s^{-1}$, which is representative of a relatively low rate at the MD scale, the stress increases continuously with strain to reach a threshold, then fluctuates around a constant value. While for other higher strain rates, the stress exhibits an overshoot before the onset of stable plastic flow. This stress overshoot is consistent with the dynamic experimental results shown in Figs. 3 and 6, which is also observed for other nanocrystal metals. For each temperature, the flow stress increases apparently with the increase of strain rate from $5 \times 10^7\ s^{-1}$ to $5 \times 10^9\ s^{-1}$, implying a significant strain rate strengthening effect. The further increase of the strain rate to more than $10^{10}\ s^{-1}$ cannot increase the flow stress anymore, suggesting a strength limit of dislocation governed plastic flow.

Fig. 10 shows the variation of the Shockley partial dislocations density at different strain rates and temperatures. Again, it shows a similar strain rate effect of dislocation behaviors between the room temperatures and cryogenic temperatures. Before the onset of plastic flow (strain below 6%), the density of partial dislocations decreases with increasing strain rate, suggesting that the nucleation of partial

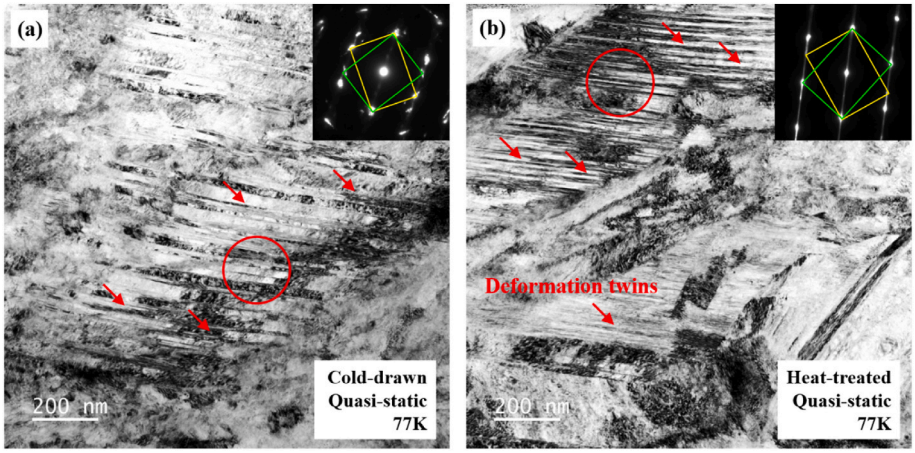

Fig. 7. TEM bright-field micrographs of (a) cold-drawn and (b) heat-treated CoCrNi wires after quasi-static tensile at 77 K.

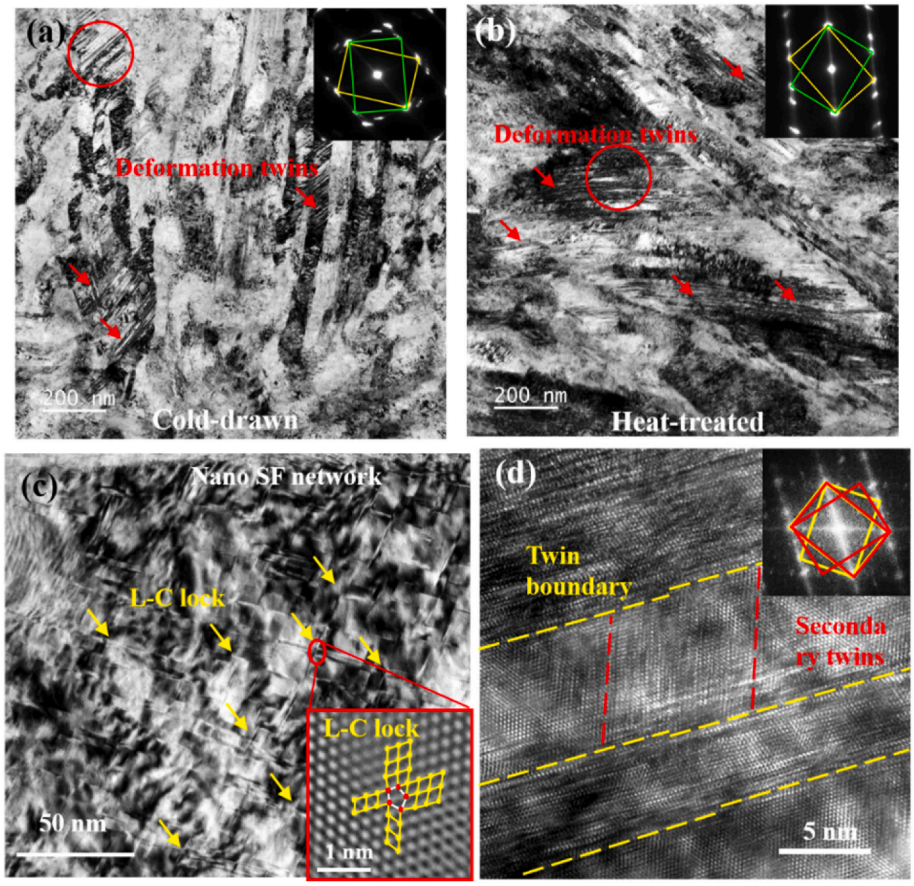

Fig. 8. TEM bright-field micrographs of (a) cold-drawn and (b) heat-treated CoCrNi MEA wires after dynamic tensile at 77 K, and (c) enlarged image of the red circle region on Fig. 8b show nano stacking fault net (d) high-resolution TEM images of the secondary twin. (For interpretation of the references to color in this figure legend, the reader is referred to the Web version of this article.)

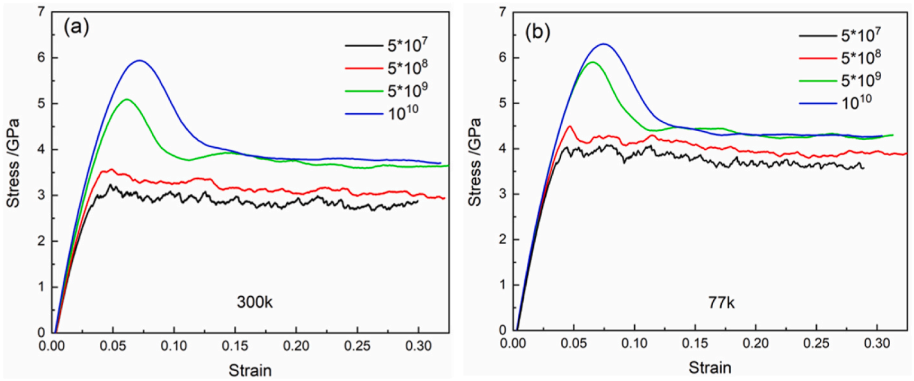

Fig. 9. MD simulated stress–strain curves for nanocrystalline CoCrNi at (a) room temperature and (b) cryogenic temperature.

dislocations have suppressed at a higher strain rate which would lead to a stress overshoot at yield, as shown in Fig. 9. In this light, it is expected that the stress overshoot becomes more pronounced when the strain rate increases, as confirmed in Fig. 9. The high strain rate induced short response time would also delay the propagate of partial dislocations to grain boundaries, which leads to intracrystalline dislocation pileup and thus increase of partial dislocation density. Therefore, in the stable flow regime, the density of partial dislocations and thus flow stress (Figs. 9, Fig.6, and Fig.3) increase with increasing strain rate.

Fig. 10 also reveals that the dislocation densities at low temperatures are slightly lower than room temperature before yielding. This result is related to the thermal activation mechanism of dislocation nucleation and proliferation, exhibiting an inhibited dislocation behavior at low temperatures. Higher stress is required for active dislocation at low temperatures [73], resulting in a higher yield and flow stress. Besides, the low activity of dislocation at low temperature would also suppress the dislocation annihilation processes such as dynamic recovery and grain boundary absorption, resulting in a higher dislocation density at high strain (>0.2, as shown in Fig. 10).

It should be noted that the densities of Shockley partial dislocation analyzed above are contributed by both stacking fault and twins. To quantitatively describe the influence of strain rate and temperature on the deformation behaviors, the variation of the atom fraction in twin boundaries and stacking faults with strain at different strain rates and

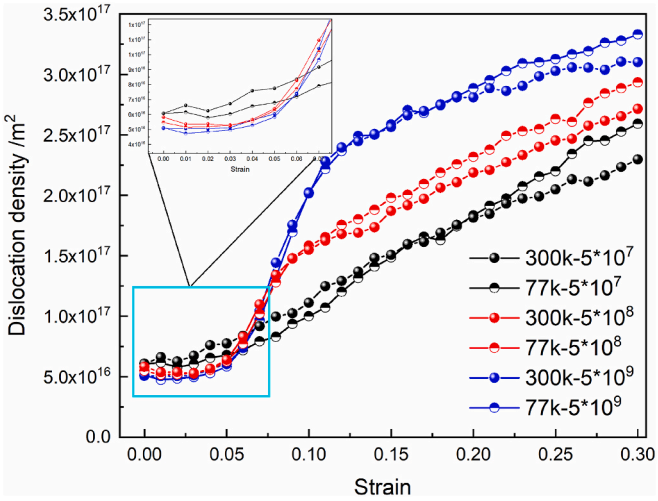

Fig. 10. Shockley partial dislocation density versus strain for different strain rates and temperature obtained by MD simulation.

temperature has been calculated. First, the FCC atoms are detected and omitted. The rest hcp atoms having a coordination number equal to six and nine belong to twin boundary and stacking faults ribbons, respectively. The results are present in Fig. 11. As shown in Fig. 11a, at an early stage of plastic deformation (strain <0.15), the fraction of stacking fault atoms increased rapidly, suggesting a rapid expansion of stacking faults caused by the movement of partial dislocation. Also note that the stacking fault ribbons decrease with increasing strain rate and decreasing temperature, suggesting limited dislocation mobility at high strain rate and low temperature. The low mobility of dislocation leads to high flow stress, as shown in Fig. 9. In light of this, the increasing dislocation density with strain rate at this stage (see Fig. 10) is derived from the explosive nucleation of partial dislocation caused by high stress (see Fig. 11).

After this expansion stage, the atoms in stacking fault ribbons are kept at a constant value, suggesting a dynamic equilibrium between annihilation and nucleation of partial dislocation. At this stage, no significant difference of stacking fault atoms was found between different temperatures and strain rates, suggesting a similar stacking fault fraction between them. This seems to signify similar mobility and thus stress among different temperatures and strain rates, contradicting the results shown in Fig. 9. However, the effect of twins cannot be ignored at this stage. As shown in Fig. 11b, at strain above 0.15, the effect of temperature and strain rate on twining becomes more and more distinguishable. Obviously, the tendency to twin increases with the strain rate regardless of temperature. Therefore, the increase of strain rate will increase the flow stress to trigger the twinning nucleation. A closer look reveals that the twin boundary fraction at low temperature is much higher than room temperature, suggests that decreasing temperature to 77 k can facilitate twinning more effectively. These results are in agreement with experimental observations. Sufficient nanotwins are well accepted as an effective strengthening and toughening mechanism for metals. Specially, it validly spans a wide temperature range in CoCrNi-based MEA/HEAs [37]. This distinguishes the HEA wires from pearlite or ferrite wires, suggesting an excellent potential for safety-critical, load-bearing applications over a wider temperature range [37].

4. Discussion

Thanks to the high-density entangled dislocations after heavy cold drawing, the cold-drawn wire has achieved an ultrahigh-strength of ~1.9 GPa at room temperature, which can further improve by decreasing to cryogenic temperature or increasing strain rate. This strength is much higher than that of CoCrNi bulk materials, as demonstrated in Table 1 where the quasi-static mechanical properties of our CoCrNi wires and reported bulk CoCrNi materials at both room temperature and 77 K are listed. Table 1 also shows that the tensile properties of both CoCrNi wires and CoCrNi bulk materials are sensitive to the hot working conditions that determine the microstructure. Slone et al. [74,75] found a strong relationship between the tensile properties and recrystallized fraction in the equiatomic CoCrNi alloy. By producing partially recrystallized heterogeneous microstructures, they have dramatically increased the yield strength to ~1100 MPa with only modest compromises to ductility in the CoCrNi alloy. This value is comparable to the strength of our heat-treated wires under the same loading conditions. Unlike these partially recrystallized heterogeneous microstructures, our heat treated wire retains the nanocrystalline structure without obvious recrystallization benefiting by the dislocation recovery treatment, as mentioned earlier (Fig. 2c). In this case, the high strength of the heat-treated CoCrNi wire originates from its entangled dislocation cells and nanotwins formed during cold drawing.

As expected, CoCrNi wires with nanocrystalline have better strength and toughness at 77 K compared to room temperature, which are consistent well with bulk CoCrNi materials with micron grain size or heterogeneous grain structures [30,32,41,76]. Both experimental and atomic simulations demonstrated an enhanced twinning activity at cryogenic temperature than at room temperature, which improves the work hardening ability and thus strength and plasticity. Besides nano-twin, HCP phase has been also observed in CoCrNi MEA during quasi-static deformation which are more prominent at cryogenic temperature [74,75]. Miao et al. [76] indicated that the enhanced nanotwin-HCP lamellae may be responsible for the improved strength and ductility at cryogenic temperature. In our study, HCP phases can

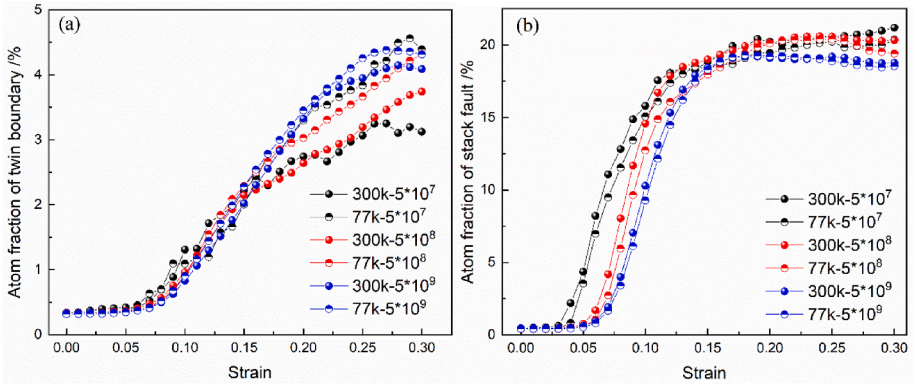

Fig. 11. Strain rate and temperature depended structural evolution (a) Fraction of atoms at twin boundaries as a function strain (b) Fraction of atoms in intrinsic stacking fault ribbons versus strain.

Table 1
Quasi-static tensile properties of CoCrNi MEA with different processing states.

Alloy	Processing steps	Yield Strength (MPa)		Tensile Strength (MPa)		fracture strain (1)		Ref.
		293 K	77 K	293 K	77 K	293 K	77 K	
CoCrNi wire	Cold-drawn to 1 mm	–	–	1938	2475	–	–	This work
	Cold-drawn to 1 mm + 873 K/1 h + 673K/2 h	1062	1259	1187	1617	0.16	0.24	
	Hot-drawn to 2 mm	1100	1515	1220	1783	0.18	0.33	[41]
CoCrNi bulk	Cold rolling (CR) ~90%+ 1198 K 1 h	318	539	853	1242	0.67	0.77	[76]
	CR ~60% + 1073k/1 h	440	657	884	1311	0.73	0.90	[30]
	Swaging+1173/1 h	360	870	560	1230	0.38	0.45	[32]
	CR: 70%	–	–	1306	–	–	–	[75]
	CR: 70% +873 K 1 h	1112	–	1272	–	0.23	–	
	CR: 70% +873 K 4 h	797	–	1101	–	0.34	–	
	CR: 70% +973 K 1 h	597	–	1013	–	0.52	–	
	CR: 70% +1173 K 1 h	346	–	854	–	0.76	–	

also be observed in the CoCrNi MEA wires before and after tensile deformation for both cold-drawn and heat-treated states. As shown in Fig. 12, these HCP phases are form in association with nanotwins, leading to the formation of nanotwin-HCP composite lamellae that are well defined by Miao et al. [76]. Experimentally, it is hardly intuitive to compare the amount and contribution of these nanotwin-HCP lamellae under different loading conditions, since it is challenging to distinguish whether they are stem from cold drawn or mechanical test. Although the formation of the HCP phase was also observed in our MD simulations, we also failed to find an obvious quantitative difference between different loading conditions. This may be caused by the relatively small strain in our MD simulations. Nonetheless, it is undoubtedly that formation of the HCP phase creates strong barriers to dislocation slip which contribute to the improvement of strength in these NiCoCr wires.

Both the TEM characterizations and MD simulations reveal that the increased strength and ductility at high strain and low temperature result from the multiplication and thinning of nanoscale twins, which further induces additional strengthening and toughening mechanisms such as stack faulting net and secondary twin. To further explore the mechanisms related to the increasing twinning as temperature decreases

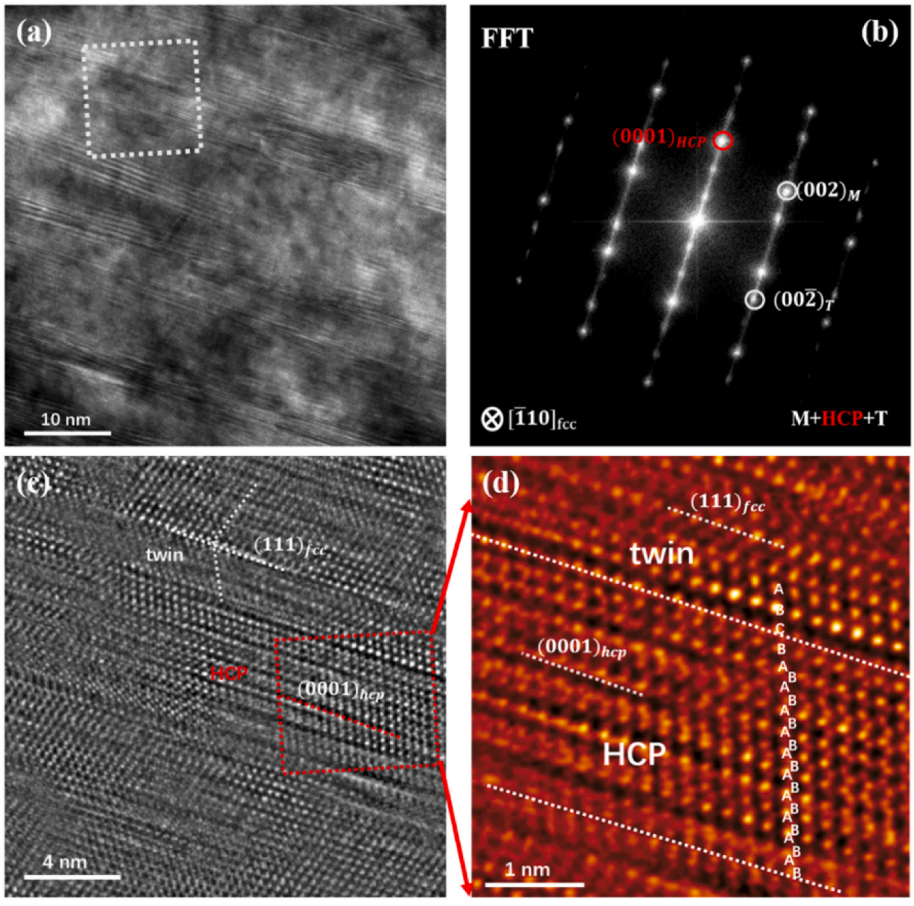

Fig. 12. HCP structures observed in CoCrNi wires: (a) high-resolution TEM image show HCP phase and (b) corresponding diffraction spots (c) well-developed nanotwin-HCP lamella and (d) atomic structure of HCP phase.

and strain rate increases, we compare the deformed atomic configurations with a strain of 0.15, where stacking faults are saturation while the amount of twinning began to bifurcate at different strain rates and temperatures, the results are shown in Fig. 13. As shown in Fig. 13a, when the sample is deformed at room temperature and a relatively low strain rate ($5 \times 10^7 s^{-1}$), stacking faults are mainly parallel in each grain and nanotwins are formed by the sequent moved partial dislocation at adjacent slip planes (denoted by white arrows). Increasing strain rate to $10^{10} s^{-1}$ or decreasing temperature to 77 K results in activation of more slip directions, in which many stacking faults intersect with each other forming stack fault networks (Fig. 13b and c). These intersected stacking faults are usually obstacles to the motion of the partial dislocations, severing as another strengthen mechanism. Additionally, these intersected stacking faults appear to guide dislocation motion parallel to the immobile stacking faults in the stack fault networks [77]. This encourages the twinning formation by overlapping the stacking faults due to the partial dislocation moving at adjacent slip planes. As denoted by yellow arrows in Fig. 13, many twins are nucleated from these intersections. In this light, the increasing stacking fault intersections were an important reason for the increasing twining at high strain rates and low temperatures.

Besides, the grain boundary is another important twin nucleation point. As marked by black arrows, many twins are emissive from grain boundaries. As demonstrated by Zhu et al. [78], the multiplication of partial dislocations at grain boundaries will supply a twinning partial on every successive slip plane for twin nucleation and growth in NC FCC materials. Rida et al. [70] suggested that this multiplication process of partial dislocations required high atomic mobility on grain boundaries. In Fig. 13, the initial grain boundaries in the initial configuration are superposed on the snapshots and marked by blue. As shown in Fig. 13a, the grain boundary and triple junction are migrated at the strain rate of 5×10^7 s^{-1} at room temperature (marked by a yellow circle). However, when the strain rate increases to 10^{10} s^{-1}, the grain boundaries position is roughly frozen while the thickness of the grain boundaries are increased. The broadening of grain boundaries is favorable for grain boundary dislocation nucleation that can promote twinning formation. This also contributes to the high twinning fraction at a high strain rate. By the way, the broadened grain boundary can also suppress grain boundary micro-cracking, which improves the ductility, as shown in Figs. 4 and 7.

Only decrease temperature to 77 K but hold a low strain rate at 5×10^7 s^{-1} cannot broadengrain boundary but can suppress grain boundary migration, as shown in Fig. 13c. In this case, GB-promoted twinning may enhance by the high yield stress and low stacking fault at low temperature. The reduction of stacking fault energy caused by low temperature also facilitates the intracrystalline twinning formation [31,79]. Therefore, the amount of twinning is increased compared to room temperature, as observed by experimental and simulation. Under the coupling of high strain rate and low temperature, the intersection stacking faults can be observed in almost every grain, as shown in Fig. 13d. This result is consistent well with the experimental observed stacking faults networks in the sample after dynamic tensile at 77 K with a strain rate of $10^3 s^{-1}$. The presence of such densen stacking fault networks greatly increase the possibility of twins. On this condition, grain boundary also broadening which further promote twinning formation, as shown in Fig. 13.

5. Conclusion

In the present study, deformation behaviors of the 1 mm CoCrNi MEA wires upon quasi-static and dynamic tension at both room and cryogenic temperature were investigated by using a novel SHTB based impact tension method for high-strength metallic wire. The TEM characterization was employed to investigate dislocation and twin substructures to uncover micro-mechanisms under different tension conditions. The main conclusions are summarized as follows:

(1) Accurate dynamic stress-strain curves of the wires can be obtained by employing the especially-designed two types of wedge clamps. The sleeve-type wedge-shaped clamp is suitable for holding high-strength and low-plastic wire samples, and the square bolt-type wedge-shaped clamp can clamp high-plastic wire samples.
(2) The cold-drawn wire exhibits an ultrahigh-strength of ~2662 MPa at cryogenic temperature and dynamic tension, resulting from the high-density entangled dislocations and deformation twins. However, high-density dislocations inhibit dislocation motion and lead to poor ductility.

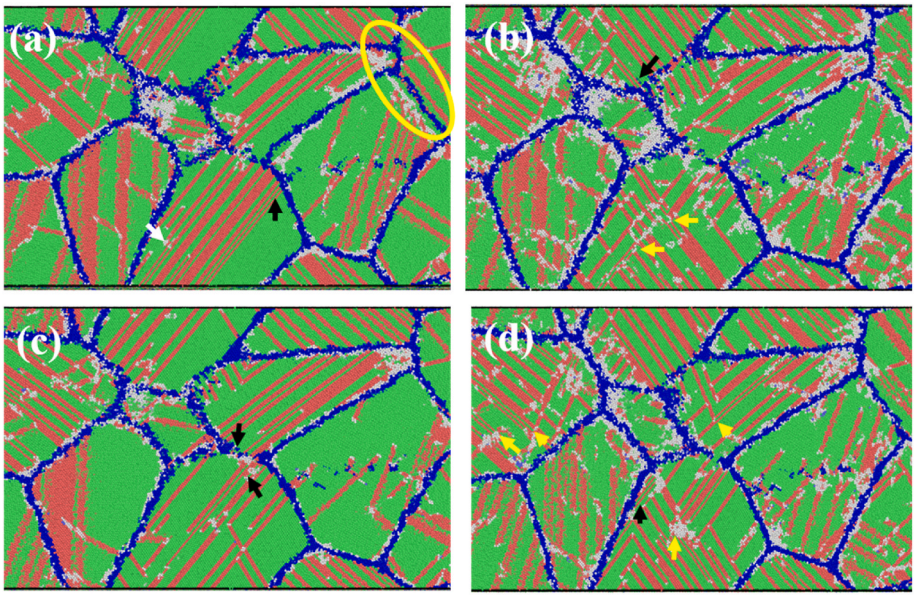

Fig. 13. A zoom on two grains inside the MEA sample at a constant strain of 15% and different strain rate and temperature (a) 300 K, 5×10^7 s^{-1} (b) 300 K, 10^{10} s^{-1} (c) 77 K, 5×10^7 s^{-1} (d) 77 K, 10^{10} s^{-1}. Atoms are colored by the common neighbor analysis. green: fcc, read: hcp, white: defect. The blue atoms are the grain boundary atoms at initial configurations. (For interpretation of the references to color in this figure legend, the reader is referred to the Web version of this article.)

(3) The current CoCrNi wire can achieve a good combination of high strength (1617 MPa) and large engineering elongation (35%) via a two-step heat treatment that lower dislocation density and maintain the nanocrystalline structure. Both high strain rate and cryogenic temperature can improve strength and plasticity simultaneously for these heat-treated wires.
(4) The enhanced mechanical property mainly results from the increasing twinning by increasing strain rate or/and decreasing temperature. In particular, coupled high strain rate and cryogenic temperature lead to abundant nanoscale twins and secondary twins, further increasing ductility and strength.
(5) On the atomic scale, the increased twinning at a high strain rate is related to the increased stack fault intersections due to multidirectional slip, which is amplified by further decreasing temperature to cryogenic temperature.

CRediT authorship contribution statement

Yu Qiao: Data curation, Investigation, Formal analysis, Writing – original draft, Writing – review & editing. **Fu-Hua Cao:** Sample preparation, Writing – review & editing, Formal analysis. **Yan Chen:** Writing – review & editing, Formal analysis. **Hai-Ying Wang:** Writing – review & editing, Formal analysis. **Lan-Hong Dai:** Conceptualization, Methodology, Funding acquisition, Supervision, Writing – review & editing.

Declaration of competing interest

The authors declare that they have no known competing financial interests or personal relationships that could have appeared to influence the work reported in this paper.

Data availability

Data will be made available on request.

Acknowledgment

This research was supported by the NSFC (Nos. 11790292, 12102433 and 11972346), the NSFC Basic Science Center Program for “Multiscale Problems in Nonlinear Mechanics” (Grant No. 11988102), Ye Qisun Science Foundation of National Natural Science Foundation of China (No. U2141204), the Key Research Program of Frontier Sciences of the Chinese Academy of Sciences (No. QYZDJSSW-JSC011), the opening project of State Key Laboratory of Explosion Science and Technology (Beijing Institute of Technology, No. KFJJ18-14 M).

Appendix A. Supplementary data

Supplementary data to this article can be found online at https://doi.org/10.1016/j.msea.2022.144041.

References

[1] M. Zelin, Microstructure evolution in pearlitic steels during wire drawing, Acta Mater. 50 (17) (2002) 4431–4447.
[2] C. Borchers, R. Kirchheim, Cold-drawn pearlitic steel wires, Prog. Mater. Sci. 82 (2016) 405–444.
[3] D. Elata, R. Eshkenazy, M.P. Weiss, The mechanical behavior of a wire rope with an independent wire rope core, Int. J. Solid Struct. 41 (5–6) (2004) 1157–1172.
[4] J. Wei, J. Li, C.Q. Wu, Behaviour of hollow-core and steel wire mesh reinforced ultra-high performance concrete columns under lateral impact loading, Int. J. Impact Eng. 146 (2020), 103726.
[5] S.W. Liu, Y.H. Sun, X.Y. Jiang, Y.H. Kang, A review of wire rope detection methods, sensors and signal processing techniques, J. Nondestr. Eval. 39 (4) (2020) 1–18.
[6] L.C. Zhou, F. Fang, M. Kumagai, E. Pickering, T.B. Yu, X.D. Zhang, Structure restoration and coarsening of nanocrystalline cementite in cold drawn pearlitic wire induced by low temperature annealing, Scripta Mater. 215 (2022), 114696.
[7] D.S. Wei, L.F. Wang, X.J. Hu, X.Y. Mao, Z.H. Xie, F. Fang, Effect of drawing strain rate on microstructure and mechanical properties of cold-drawn pearlitic steel wires, J. Mater. Sci. 57 (19) (2022) 8924–8939.
[8] Y. Li, D. Raabe, M. Herbig, P.P. Choi, S. Goto, A. Kostka, H. Yarita, C. Borchers, R. Kirchheim, Segregation stabilizes nanocrystalline bulk steel with near theoretical strength, Phys. Rev. Lett. 113 (10) (2014), 106104.
[9] L. Xiang, L.W. Liang, Y.J. Wang, Y. Chen, H.Y. Wang, L.H. Dai, One-step annealing optimizes strength-ductility tradeoff in pearlitic steel wires, Mater. Sci. Eng., A 757 (2019) 1–13.
[10] E.P. George, D. Raabe, R.O. Ritchie, High-entropy alloys, Nat. Rev. Mater. 4 (8) (2019) 515–534.
[11] E.P. George, W.A. Curtin, C.C. Tasan, High entropy alloys: a focused review of mechanical properties and deformation mechanisms, Acta Mater. 188 (2020) 435–474.
[12] E. Ma, Unusual dislocation behavior in high-entropy alloys, Scripta Mater. 181 (2020) 127–133.
[13] Z.Z. Li, S.T. Zhao, R.O. Ritchie, M.A. Meyers, Mechanical properties of high-entropy alloys with emphasis on face-centered cubic alloys, Prog. Mater. Sci. 102 (2019) 296–345.
[14] J.W. Yeh, S.K. Chen, S.J. Lin, J.Y. Gan, T.S. Chin, T.T. Shun, C.H. Tsau, S.Y. Chang, Nanostructured high-entropy alloys with multiple principal elements: novel alloy design concepts and outcomes, Adv. Eng. Mater. 6 (5) (2004) 299–303.
[15] Y. Zhang, T.T. Zuo, Z. Tang, M.C. Gao, K.A. Dahmen, P.K. Liaw, Z.P. Lu, Microstructures and properties of high-entropy alloys, Prog. Mater. Sci. 61 (2014) 1–93.
[16] Q. Li, T.W. Zhang, J.W. Qiao, S.G. Ma, D. Zhao, P. Lu, B. Xu, Z.H. Wang, Superior tensile properties of Al0.3CoCrFeNi high entropy alloys with B2 precipitated phases at room and cryogenic temperatures, Mater. Sci. Eng., A (2019) 767.
[17] Z.Z. Li, S.T. Zhao, S.M. Alotaibi, Y. Liu, B.F. Wang, M.A. Meyers, Adiabatic shear localization in the CrMnFeCoNi high-entropy alloy, Acta Mater. 151 (2018) 424–431.
[18] Y.Q. Bu, H.T. Wang, Short-range order in multicomponent alloys, Advances in Mechanics 51 (4) (2021) 915–919.
[19] S.P. Wang, E. Ma, J. Xu, New ternary equi-atomic refractory medium-entropy alloys with tensile ductility: hafnium versus titanium into NbTa-based solution, Intermetallics 107 (2019) 15–23.
[20] Z.M. Li, C.C. Tasan, K.G. Pradeep, D. Raabe, A TRIP-assisted dual-phase high-entropy alloy: grain size and phase fraction effects on deformation behavior, Acta Mater. 131 (2017) 323–335.
[21] Z.F. Lei, X.J. Liu, Y. Wu, H. Wang, S.H. Jiang, S.D. Wang, X.D. Hui, Y.D. Wu, B. Gault, P. Kontis, Enhanced strength and ductility in a high-entropy alloy via ordered oxygen complexes, Nature 563 (7732) (2018) 546–550.
[22] Z.M. Li, K.G. Pradeep, Y. Deng, D. Raabe, C.C. Tasan, Metastable high-entropy dual-phase alloys overcome the strength–ductility trade-off, Nature 534 (7606) (2016) 227–230.
[23] C. Zhang, C.Y. Zhu, P.H. Cao, X. Wang, F. Ye, K. Kaufmann, L. Casalena, B. E. MacDonald, X.Q. Pan, K. Vecchio, Aged metastable high-entropy alloys with heterogeneous lamella structure for superior strength-ductility synergy, Acta Mater. 199 (2020) 602–612.
[24] Z.C. Xie, C. Li, H.Y. Wang, C.S. Lu, L.H. Dai, Hydrogen induced slowdown of spallation in high entropy alloy under shock loading, Int. J. Plast. 139 (2021), 102944.
[25] Z. Pu, Y. Chen, L.H. Dai, Strong resistance to hydrogen embrittlement of high-entropy alloy, Mater. Sci. Eng., A 736 (2018) 156–166.
[26] Y.H. Jo, S. Jung, W.M. Choi, S.S. Sohn, H.S. Kim, B.J. Lee, N.J. Kim, S. Lee, Cryogenic strength improvement by utilizing room-temperature deformation twinning in a partially recrystallized VCrMnFeCoNi high-entropy alloy, Nat. Commun. 8 (2017), 15719.
[27] X.F. Liu, Z.L. Tian, X.F. Zhang, H.H. Chen, T.W. Liu, Y. Chen, Y.J. Wang, L.H. Dai, Self-sharpening" tungsten high-entropy alloy, Acta Mater. 186 (2020) 257–266.
[28] Q.Q. Ding, X.Q. Fu, D.K. Chen, H.B. Bei, B. Gludovatz, J.X. Li, Z. Zhang, E. P. George, Q. Yu, T. Zhu, R.O. Ritchie, Real-time nanoscale observation of deformation mechanisms in CrCoNi-based medium- to high-entropy alloys at cryogenic temperatures, Mater. Today 25 (2019) 21–27.
[29] P. Gao, Z.H. Ma, J. Gu, S. Ni, T. Suo, Y.L. Li, M. Song, Y.W. Mai, X.Z. Liao, Exceptional high-strain-rate tensile mechanical properties in a CrCoNi medium-entropy alloy, Science China Materials 65 (3) (2021) 811–819.
[30] B. Gludovatz, A. Hohenwarter, K.V. Thurston, H. Bei, Z. Wu, E.P. George, R. O. Ritchie, Exceptional damage-tolerance of a medium-entropy alloy CrCoNi at cryogenic temperatures, Nat. Commun. 7 (2016), 10602.
[31] S. Huang, W. Li, S. Lu, F.Y. Tian, J. Shen, E. Holmström, L. Vitos, Temperature dependent stacking fault energy of FeCrCoNiMn high entropy alloy, Scripta Mater. 108 (2015) 44–47.
[32] G. Laplanche, A. Kostka, C. Reinhart, J. Hunfeld, G. Eggeler, E.P. George, Reasons for the superior mechanical properties of medium-entropy CrCoNi compared to high-entropy CrMnFeCoNi, Acta Mater. 128 (2017) 292–303.
[33] G. Laplanche, J. Bonneville, C. Varvenne, W.A. Curtin, E.P. George, Thermal activation parameters of plastic flow reveal deformation mechanisms in the CrMnFeCoNi high-entropy alloy, Acta Mater. 143 (2018) 257–264.
[34] G. Laplanche, A. Kostka, O.M. Horst, G. Eggeler, E.P. George, Microstructure evolution and critical stress for twinning in the CrMnFeCoNi high-entropy alloy, Acta Mater. 118 (2016) 152–163.
[35] Y. Qiao, Y. Chen, F.H. Cao, H.Y. Wang, L.H. Dai, Dynamic behavior of CrMnFeCoNi high-entropy alloy in impact tension, Int. J. Impact Eng. 158 (2021), 104008.
[36] D.Y. Li, C.X. Li, T. Feng, Y.D. Zhang, G. Sha, J.J. Lewandowski, P.K. Liaw, Y. Zhang, High-entropy Al0.3CoCrFeNi alloy fibers with high tensile strength and ductility at ambient and cryogenic temperatures, Acta Mater. 123 (2017) 285–294.

[37] W. Huo, F. Fang, H. Zhou, Z.H. Xie, J.K. Shang, J.Q. Jiang, Remarkable strength of CoCrFeNi high-entropy alloy wires at cryogenic and elevated temperatures, Scripta Mater. 141 (2017) 125–128.
[38] S.H. Shim, H. Pouraliakbar, S.I. Hong, High strength dual fcc phase CoCuFeMnNi high-entropy alloy wires with dislocation wall boundaries stabilized by phase boundaries, Mater. Sci. Eng., A 825 (2021), 141875.
[39] Y.J. Kwon, J.W. Won, S.H. Park, J.H. Lee, K.R. Lim, Y.S. Na, C.S.J.M.S. Lee, E. A, Ultrahigh-strength CoCrFeMnNi high-entropy alloy wire rod with excellent resistance to hydrogen embrittlement, Mater. Sci. Eng., A 732 (2018) 105–111.
[40] J.X. Chen, Y. Chen, J.P. Liu, T.W. Liu, L.H. Dai, Anomalous size effect in micron-scale CoCrNi medium-entropy alloy wire, Scripta Mater. 199 (2021), 113897.
[41] J.P. Liu, J.X. Chen, T.W. Liu, C. Li, Y. Chen, L.H. Dai, Superior strength-ductility CoCrNi medium-entropy alloy wire, Scripta Mater. 181 (2020) 19–24.
[42] L.S. Mantha, B.E. MacDonald, X. Mu, A. Mazilkin, J. Ivanisenko, H. Hahn, E. J. Lavernia, S. Katnagallu, C. Kübel, Grain boundary segregation induced precipitation in a non equiatomic nanocrystalline CoCuFeMnNi compositionally complex alloy, Acta Mater. 220 (2021), 117281.
[43] Y. Lu, A. Mazilkin, T. Boll, N. Stepanov, S. Zherebtzov, G. Salishchev, É. Ódor, T. Ungar, E. Lavernia, H. Hahn, Influence of carbon on the mechanical behavior and microstructure evolution of CoCrFeMnNi processed by high pressure torsion, Materialia 16 (2021), 101059.
[44] Y.X. Peng, X.D. Chang, S.S. Sun, Z.C. Zhu, X.S. Gong, S.Y. Zou, W.X. Xu, Z.T. Mi, The friction and wear properties of steel wire rope sliding against itself under impact load, Wear 400–401 (2018) 194–206.
[45] M. Bateman, I. Howard, A. Johnson, J. Walton, Computer simulation of the impact performance of a wire rope safety fence, Int. J. Impact Eng. 25 (1) (2001) 67–85.
[46] P.V. Tran, K. Maegawa, S. Fukada, Prototype of a wire-rope rockfall protective fence developed with three-dimensional numerical modeling, Comput. Geotech. 54 (2013) 84–93.
[47] B. Hopkinson, The effects of momentary stresses in metals, Proceedings of the Royal Society of London. Series A: Mathematica 74 (497) (1905) 498–506.
[48] C.Z. Wang, H.X. Wang, K. Shankar, E.V. Morozov, P.J. Hazell, On the mechanical behaviour of steel wire mesh subjected to low-velocity impact, Thin-Walled Struct. 159 (2021), 107281.
[49] C.Z. Wang, H.X. Wang, K. Shankar, P.J. Hazell, Dynamic failure behavior of steel wire mesh subjected to medium velocity impact: experiments and simulations, Int. J. Mech. Sci. 216 (2022), 106991.
[50] T.W. Zhang, S.G. Ma, D. Zhao, Y.C. Wu, Y. Zhang, Z.H. Wang, J.W. Qiao, Simultaneous enhancement of strength and ductility in a NiCoCrFe high-entropy alloy upon dynamic tension: micromechanism and constitutive modeling, Int. J. Plast. 124 (2020) 226–246.
[51] S. Ma, Z. Jiao, J. Qiao, H. Yang, Y. Zhang, Z. Wang, Strain rate effects on the dynamic mechanical properties of the AlCrCuFeNi2 high-entropy alloy, Mater. Sci. Eng., A 649 (2016) 35–38.
[52] B. Song, W.W. Chen, W.Y. Lu, Mechanical characterization at intermediate strain rates for rate effects on an epoxy syntactic foam, Int. J. Mech. Sci. 49 (12) (2007) 1336–1343.
[53] Y. Qiao, P.F. Wang, X. Xue, M. Liu, S.L. Xu, Enhancing the dynamic temperature stability of epoxy with graphene oxide, Mech. Mater. 150 (2020), 103593.
[54] S. Plimpton, Fast parallel algorithms for short-range molecular dynamics, J. Comput. Phys. 117 (1) (1995) 1–19.
[55] Q.J. Li, H. Sheng, E. Ma, Strengthening in multi-principal element alloys with local-chemical-order roughened dislocation pathways, Nat. Commun. 10 (1) (2019) 1–11.
[56] S. Melchionna, G. Ciccotti, B. Lee Holian, Hoover NPT dynamics for systems varying in shape and size, Mol. Phys. 78 (3) (1993) 533–544.
[57] A. Stukowski, Visualization and analysis of atomistic simulation data with OVITO–the Open Visualization Tool, Modelling simulation in materials science engineering fracture mechanics 18 (1) (2009), 015012.
[58] P.M. Larsen, S. Schmidt, J. Schiøtz, Robust structural identification via polyhedral template matching, Modelling simulation in materials science engineering fracture mechanics 24 (5) (2016), 055007.
[59] X.D. Zhang, A. Godfrey, N. Hansen, X.X. Huang, Hierarchical structures in cold-drawn pearlitic steel wire, Acta Mater. 61 (13) (2013) 4898–4909.
[60] G.Q. Ma, D.A. Hughes, A.W. Godfrey, Q. Chen, N. Hansen, G.L. Wu, Microstructure and strength of a tantalum-tungsten alloy after cold rolling from small to large strains, J. Mater. Sci. Technol. 83 (2021) 34–48.
[61] Y.H. Zhao, T. Topping, J.F. Bingert, J.J. Thornton, A.M. Dangelewicz, Y. Li, W. Liu, Y.T. Zhu, Y.Z. Zhou, E.J. Lavernia, High tensile ductility and strength in bulk nanostructured nickel, Adv. Mater. 20 (16) (2008) 3028–3033.
[62] W.G. Johnston, J.J. Gilman, Dislocation velocities, dislocation densities, and plastic flow in lithium fluoride crystals, J. Appl. Phys. 30 (2) (1959) 129–144.
[63] Z.B. Zheng, N.G. Prastiti, D.S. Balint, F.P.E. Dunne, The dislocation configurational energy density in discrete dislocation plasticity, J. Mech. Phys. Solid. 129 (2019) 39–60.
[64] S. Ni, Y.B. Wang, X.Z. Liao, R.B. Figueiredo, H.Q. Li, S.P. Ringer, T.G. Langdon, Y. T. Zhu, The effect of dislocation density on the interactions between dislocations and twin boundaries in nanocrystalline materials, Acta Mater. 60 (6–7) (2012) 3181–3189.
[65] Z.G. Wu, Y.F. Gao, H.B. Bei, Thermal activation mechanisms and Labusch-type strengthening analysis for a family of high-entropy and equiatomic solid-solution alloys, Acta Mater. 120 (2016) 108–119.
[66] W. Woo, M. Naeem, J.S. Jeong, C.M. Lee, S. Harjo, T. Kawasaki, H. He, X.L. Wang, Comparison of dislocation density, twin fault probability, and stacking fault energy between CrCoNi and CrCoNiFe medium entropy alloys deformed at 293 and 140K, Mater. Sci. Eng., A 781 (2020), 139224.
[67] D. Bufford, Z. Bi, Q.X. Jia, H. Wang, X. Zhang, Nanotwins and stacking faults in high-strength epitaxial Ag/Al multilayer films, Appl. Phys. Lett. 101 (22) (2012).
[68] H.K. Cho, J.Y. Lee, K.S. Kim, G.M. Yang, Superlattice-like stacking fault and phase separation of InxGa1−xN grown on sapphire substrate by metalorganic chemical vapor deposition, Appl. Phys. Lett. 77 (2) (2000) 247–249.
[69] Z. Zhang, H. Sheng, Z. Wang, B. Gludovatz, Z. Zhang, E.P. George, Q. Yu, S.X. Mao, R.O. Ritchie, Dislocation mechanisms and 3D twin architectures generate exceptional strength-ductility-toughness combination in CrCoNi medium-entropy alloy, Nat. Commun. 8 (2017), 14390.
[70] A. Rida, M. Micoulaut, E. Rouhaud, A. Makke, Understanding the strain rate sensitivity of nanocrystalline copper using molecular dynamics simulations, Comput. Mater. Sci. 172 (2020), 109294.
[71] D. Wolf, V. Yamakov, S. Phillpot, A. Mukherjee, H. Gleiter, Deformation of nanocrystalline materials by molecular-dynamics simulation: relationship to experiments? Acta Mater. 53 (1) (2005) 1–40.
[72] T. Zhang, K. Zhou, Z. Chen, Strain rate effect on plastic deformation of nanocrystalline copper investigated by molecular dynamics, Mater. Sci. Eng., A 648 (2015) 23–30.
[73] T. Zhu, J. Li, A. Samanta, A. Leach, K. Gall, Temperature and strain-rate dependence of surface dislocation nucleation, Phys. Rev. Lett. 100 (2) (2008), 025502.
[74] C.E. Slone, S. Chakraborty, J. Miao, E.P. George, M.J. Mills, S.R. Niezgoda, Influence of deformation induced nanoscale twinning and FCC-HCP transformation on hardening and texture development in medium-entropy CrCoNi alloy, Acta Mater. 158 (2018) 38–52.
[75] C.E. Slone, J. Miao, E.P. George, M.J. Mills, Achieving ultra-high strength and ductility in equiatomic CrCoNi with partially recrystallized microstructures, Acta Mater. 165 (2019) 496–507.
[76] J. Miao, C.E. Slone, T.M. Smith, C. Niu, H. Bei, M. Ghazisaeidi, G.M. Pharr, M. J. Mills, The evolution of the deformation substructure in a Ni-Co-Cr equiatomic solid solution alloy, Acta Mater. 132 (2017) 35–48.
[77] S.J. Chen, H.S. Oh, B. Gludovatz, S.J. Kim, E.S. Park, Z. Zhang, R.O. Ritchie, Q. Yu, Real-time observations of TRIP-induced ultrahigh strain hardening in a dual-phase CrMnFeCoNi high-entropy alloy, Nat. Commun. 11 (1) (2020) 1–8.
[78] Y. Zhu, X. Wu, X. Liao, J. Narayan, S. Mathaudhu, L. Kecskes, Twinning partial multiplication at grain boundary in nanocrystalline fcc metals, Appl. Phys. Lett. 95 (3) (2009), 031909.
[79] S. Hayakawa, H.X. Xu, Temperature-dependent mechanisms of dislocation–twin boundary interactions in Ni-based equiatomic alloys, Acta Mater. 211 (2021), 116886.